Materials Science & Engineering A 817 (2021) 141373

Contents lists available at ScienceDirect

Materials Science & Engineering A

journal homepage: www.elsevier.com/locate/msea

Manipulating deformation mechanisms with Y alloying of Mg

Jiaxiang Wang [a,*], Xin Wang [b], Kehang Yu [b], Timothy J. Rupert [b], Subhash Mahajan [c], Enrique J. Lavernia [b], Julie M. Schoenung [b], Irene J. Beyerlein [a,d]

[a] University of California, Santa Barbara, Department of Mechanical Engineering, USA
[b] University of California, Irvine, Department of Materials Science and Engineering, USA
[c] University of California, Davis, Department of Materials Science and Engineering, USA
[d] University of California, Santa Barbara, Materials Department, USA

ARTICLE INFO

Keywords:
A. Electron microscopy
A. Simulation
A. Stress/strain measurement
B. Magnesium alloys
D. Plasticity

ABSTRACT

The effect of Y concentration on the slip and twinning mechanisms in binary Mg–Y alloys are investigated using transmission electron microscopy, electron backscattered diffraction, and visco-plastic self-consistent polycrystal constitutive modeling. Four concentrations of Y are studied in hot-rolled and recrystallized sheet material. The materials were deformed in tension and compression in the rolling direction and compression in the normal direction in order to invoke distinct proportions of slip and twin mechanisms with each test. Within the single crystal hardening model used in polycrystal modeling, a slip-twin interaction law is introduced to account for dislocation density reductions due to dislocation absorption during twin boundary migration. We show that increasing Y concentration reduces the intensities of both the initial and deformation textures. During deformation, the plastic anisotropy in yield stress, the tension-compression asymmetry, and amount of $\{10\bar{1}2\}\langle\bar{1}011\rangle$ twinning is shown to decrease with increasing Y. For each alloy, the model identifies a single set of material parameters that successfully reproduced all measured stress-strain curves and achieved agreement with measured deformation textures and twin area fractions. Transcending texture effects, the model interpretation of the flow responses suggests that increased concentrations of Y increase the critical resolved shear stress for basal slip but have negligible effects on the other slip modes. The reduced plastic anisotropy with increases in Y is explained by a concomitant decrease in the prismatic-to-pyramidal slip critical resolved shear stress ratio. The model suggests that their nearly equivalent critical resolved shear stress values lead to the enhanced non-basal activity of Mg–Y alloys, which was confirmed by transmission electron microscopy. The calculations suggest that beyond any texture differences, this reduction in twinning can be attributed to a slightly increased resistance for $\{10\bar{1}2\}\langle\bar{1}011\rangle$ twin propagation, particularly in the binary with the highest Y content.

1. Introduction

Mg alloys have been the focus of intense research in recent years due to their potential for light weighting structural components. The challenge, however, is that Mg and its alloys display some undesirable mechanical properties, such as strong plastic anisotropy [1], tension/compression asymmetry [2,3] and limited room temperature ductility [4,5], which limit their widespread application. Mg has a hexagonal close packed (HCP) crystal structure and tends to deform by two distinct deformation mechanisms, dislocation slip and deformation twinning, both of which are intrinsically anisotropic due to the low crystallographic symmetry. The easiest dislocations to activate in Mg are basal <a> dislocations but they only accommodate <a> axis deformation. Pyramidal <c+a> dislocations can accommodate strain along the <c> axis but are more difficult to move, with critical resolved shear stress (CRSS) values several tens to a hundred times higher than those for basal <a> slip at room temperature [6]. Deformation twinning, on the other hand, generates polarized shear. Twins of a certain type can be activated by either <c> axis tension only or <c> axis compression only. For example, the common $\{10\bar{1}2\}\langle\bar{1}011\rangle$ twin in Mg operates under extension of the <c> axis or contraction perpendicular to the <c> axis, but not vice versa. Together, the activities and interactions of multiple slip and twinning modes determine the complicated plastic behavior of

* Corresponding author.
E-mail address: jiaxiangwang@ucsb.edu (J. Wang).

https://doi.org/10.1016/j.msea.2021.141373
Received 26 February 2021; Received in revised form 19 April 2021; Accepted 20 April 2021
Available online 5 May 2021

Mg.

One strategy to reduce the plastic anisotropy and possibly enhance the performance of Mg is to alter the activation barrier for each slip and twinning mode via alloying. Alloying elements in Mg that increase the CRSS values for basal slip or decrease those for non-basal slip tend to lower the non-basal-to-basal CRSS ratio. Enhanced formability and an increased CRSS for basal slip have been reported in Mg with additions of Al [7,8], Zn [7–9] and Sn [10]. The improved formability with the addition of Li has been attributed to a decreased CRSS for <c+a> pyramidal slip [11,12] and an increased CRSS for $\left\{10\bar{1}2\right\}\langle\bar{1}011\rangle$ twinning [13]. Moreover, even dilute additions of rare earth elements, such as Y or Ce, can significantly decrease the basal texture and enhance room temperature ductility [5,14–20]. The activity of non-basal deformation modes has been substantially enhanced by rare earth alloying. Some experimental studies have been carried out to study the effect of Y on the behavior of Mg–Y binary alloys. In related studies using transmission electron microscopy (TEM) and density functional theory (DFT) simulations, Sandlöbes et al. [21–23] reported an increased concentration of <c+a> dislocations in binary solid solution Mg–Y, where I1 stacking faults act as a heterogeneous nucleation source for <c+a> dislocations. Zhang et al. [17,18] used in-situ compression in TEM to study the CRSS values for slip and twinning modes activated in the Mg-2.5 at. % Y crystal and showed that prismatic slip was favored over $\left\{10\bar{1}2\right\}\langle\bar{1}011\rangle$ twinning in alloys with Y additions. Rikihisa et al. [24] and Takemoto et al. [25] observed that the activities of prismatic slip and first-order pyramidal slip increase with increasing Y. In examining different concentrations of Mg–Y (0.2 at.%, 0.3 at.%, 0.8 at.%, 1.2 at.% and 2.0 at.%), from ambient temperature to 350 °C, Gao et al., found that the yield strength of Mg–Y increases linearly with $c^{1/2}$ or $c^{2/3}$, where c is the atomic concentration [26]. However, for low concentrations of Y, according to Shi et al., the strengthening effect caused by solute is less than the softening effect by a weaker texture [27]. In addition, Huang et al. [19] and Zhao et al. [28] reported that the macroscopic behavior of Mg–Y is very sensitive to the initial texture and grain size.

A comprehensive understanding of the effects of alloying, including the type of alloying elements and concentrations, is desired to further guide alloy selection for high-performance Mg alloys. While many of the studies in the literature have led to important, although sometimes contradictory, findings, it is evident that revealing experimentally the intrinsic effects of alloying can be extremely challenging. There exists a large number of extrinsic variables (e.g., texture, grain size, loading direction, etc.) that each have their individual impact on deformation behavior. For instance, twin evolution affects texture by abruptly reorienting the crystals and altering the slip activity, and vice versa. In turn, differences in texture, at any stage of the deformation, can change the readiness for slip and twinning, and hence the stress-strain response, even in the same alloy. Therefore, to differentiate the individual effects of alloying, crystal plasticity modeling, which is capable of connecting the evolution of the texture to the relative contributions of each slip and twinning mode, can be helpful.

The present study aims to understand the effects of Y alloying on the plastic anisotropic deformation behavior, texture evolution, and underlying slip and twinning activity. Four Mg–Y binary solid solution alloys with nominal compositions of Mg-0.2 wt% Y (Mg-0.2Y), Mg-0.6 wt% Y (Mg-0.6Y), Mg-1 wt.% Y (Mg–1Y), and Mg-3 wt.% Y (Mg–3Y) were processed via rolling and subsequent annealing so that they all possess comparable grain sizes. Tension or compression responses were measured along three distinct orientations. To investigate their deformation mechanisms, visco-plastic self-consistent (VPSC) modeling is used to simulate the stress-strain responses along the three loading orientations and, importantly, only a single set of material-related parameters is used for each alloy, as a testament to the reliability of the model. The calculated slip activities, texture evolution and twin volume fraction evolution were then examined together with the experimental results on texture, dislocation structure and twin area fraction to shed light on the individual effects of Y additions on the activation and hardening of each slip and twinning mode.

Table 1
Nominal compositions, recrystallization heat treatment conditions and average grain size of Mg–Y alloys.

Sample	Mg-0.2Y	Mg-0.6Y	Mg–1Y	Mg–3Y
Solute concentration	0.2 wt%	0.6 wt%	1 wt%	3 wt%
Recrystallization temperature and time	400 °C, 5 min	400 °C, 10 min	400 °C, 10 min	450 °C, 10 min
Average grain size	35 μm	21 μm	22 μm	26 μm

2. Experimental methods

2.1. Material

Starting with high-purity Mg, four Mg–Y alloys (Mg-0.2Y, Mg-0.6Y, Mg–1Y and Mg–3Y) were prepared at Helmholtz-Zentrum Geesthacht in Geesthacht, Germany. The chemical composition of the alloys was controlled by spark emission spectrometry and are the same as those used in prior studies [20,29]. The cast ingots were homogenization heat-treated and hot-rolled at 500 °C to a final thickness of 6 mm. To achieve a similar grain size of approximately 20–25 μm in all four Mg–Y alloys, selected recrystallization heat treatment procedures were carried out. These recrystallization parameters for the four samples are listed in Table 1.

2.2. Mechanical testing

The four Mg–Y alloys were quasi-statically tested at room temperature under compression along the rolling direction (RD-C), compression along the normal direction (ND-C) and tension along the rolling direction (RD-T), all at room temperature. Tension and compression samples for mechanical testing were machined from the rolled sheets using electrical discharge machining (EDM). Compression samples were ~3.3 × 3.3 × 5 mm cuboids, with the compression axes along RD or ND. Dog-bone shaped tension samples had a gauge length of 20 mm along the RD and a rectangular cross section of 4 × 2 mm, following ASTM E8 standard [30]. Uniaxial tension and compression mechanical tests were performed at a constant crosshead speed with a nominal strain rate of $\sim 10^{-3}$ s^{-1} using an 8801 servo-hydraulic universal testing system (Instron Inc., USA) equipped with a dual-camera video extensometer for non-contact, high-resolution strain measurement. For the analyses of microstructure and texture evolution, mechanical tests were interrupted at various strain conditions.

2.3. Microstructural characterization

To conduct crystallographic texture analysis, pole figures of the four Mg–Y alloys were measured by a SmartLab X-ray diffractometer (XRD, Rigaku, Japan) using Cu Kα (λ = 0.1542 nm) radiation under in-plane diffraction mode. Three pole figures of {0002}, {10-10}, and {10–11} were collected for each sample and plotted using the open source MTEX software package [31]. For an investigation of the texture evolution, pole figures were measured for Mg-0.2Y samples deformed in RD-C to 5%, 7% and 13% strain and in ND-C to 10% strain, respectively. The strain values mentioned in this paper were recalculated into true strain.

To investigate the structure of pyramidal dislocations, TEM characterization of ND-C 2% pre-strained Mg–1Y samples was carried out using a JEOL JEM 2800 (JEOL, Japan) operating at 200 kV. For comparison, a 2% strain ND-compressed, commercially pure Mg sample (99.9%, Goodfellow Inc., USA) was also investigated by TEM. To prepare TEM specimens, pre-strained samples were cut into 1.0-to-1.5 mm thin foils from the center of the compression sample parallel to the ND × RD

plane. The thin foils were then mechanically ground and sequentially polished down to 1 μm diamond suspension, followed by chemical polishing in a nitric acid:ethanol = 1:9 solution for 10 s. Finally, the samples were punched into Φ 3 mm disks and ion polished to electron transparency using PIPS (Gatan Inc., USA) at approximately −100 °C, with ion-beam energies from 5 keV down to 1.5 keV and milling angles from 6° to 2°.

Electron backscatter diffraction (EBSD) maps were collected from RD-C deformed Mg–Y alloys to analyze their tendency to twin. EBSD was performed with a field emission scanning electron microscope (SEM, GAIA3, Tescan Inc., Czech Republic) operating at 20 kV, equipped with an Oxford AztecHKL NordlysMax2 integrated EBSD system. The partially deformed RD-C samples, deformed to ~5% true strain, were sectioned parallel to the RD × ND plane using EDM. For EBSD characterization, the samples were mechanically polished down to 0.05 μm colloidal silica in ethylene glycol followed by chemical etching using an etchant of nitric acid:hydrochloric acid:ethanol = 1:2:7. To get a statistically representative dataset on the deformed microstructure, EBSD maps were acquired from six 500 × 500 μm randomly selected regions for each alloy, with a scanning step size of 1 μm. Twin statistics were analyzed from the EBSD scans using QTcrystals developed by Cédric Pradalier et al. [32] to identify the twin/parent orientation relationship and calculate the twin area fractions.

3. Polycrystal plasticity constitutive modeling

The visco-plastic self-consistent (VPSC) model was employed to relate the macroscopic deformation response with texture evolution and the underlying slip and twinning mechanisms. A detailed description of the VPSC model originally developed by Lebensohn and Tomé can be found in Refs. [33,34]. We extend the hardening law used in VPSC to account for the interaction between dislocation storage and twin growth. For this reason, in this section, we briefly describe both the VPSC polycrystal model and the constitutive response it uses, which is a dislocation density based hardening law for slip and twinning systems. We follow then with the model for slip/twin interactions.

3.1. Visco-plastic self-consistent formulation

In the following model description, we let α represent the slip mode (i.e., basal, prismatic or pyramidal) and β denote the twin type. The expression $s \in \alpha$ means that the slip system s belongs to slip mode α and $t \in \beta$ the twin system t belongs to twin mode β. The flow rule of VPSC, which relates the local stress to strain rate, is expressed in the form of a power-law function via:

$$\dot{\gamma}^s = \dot{\gamma}_0 \left| \frac{m^s : \sigma}{\tau_c^s(\dot{\varepsilon}, T)} \right|^n \mathrm{sign}(m^s : \sigma) \tag{1}$$

The flow rule introduces a critical strength or slip resistance τ_c^s that depends on the local microstructure and structural obstacles encountered by the dislocations. In Eq. (1), $\dot{\gamma}^s$ and m^s are, respectively, the shear rate and the symmetric Schmid tensor for system s, $\dot{\gamma}_0$ is the reference shear strain rate, and σ is the stress tensor. The exponent n has been referred to as the inverse slip rate sensitivity, yet here we elect to use a sufficiently high value for n (i.e., $n = 20$), so that rate sensitivity in the activation of slip ($\dot{\gamma} > 0$) is controlled by the rate sensitivity in τ_c^s.

3.2. Constitutive hardening law

To define τ_c^s, we use a thermally activated dislocation density based hardening law (DD model) developed by Beyerlein and Tomé [35]. In this model, work hardening in τ_c^s is linked to the evolution of dislocations, their mutual interactions, and their interactions with barriers in the microstructure. The CRSS on slip system s, τ_c^s, is given as a sum of the contributions from forest dislocations, debris, and twin boundaries, via,

$$\tau_c^s = \tau_0^\alpha + \tau_{\mathrm{for}}^s + \tau_{\mathrm{deb}}^s + \tau_{TB}^s \; s \in \alpha \tag{2}$$

where τ_0^α is the initial slip resistance. The stress τ_{for}^s and τ_{deb}^s are the forest dislocation interaction stress and dislocation substructure interaction stress. The evolution of τ_{for}^s follows the traditional Taylor law, relating glide resistance to a forest dislocation density, i.e., $\tau_{for}^s = b^s \chi \mu \sqrt{\rho_{for}^s}$, where χ, μ, and b^s are the dislocation-interaction parameter, effective shear modulus, and value of the Burgers vector of slip system s, respectively. The parameter χ usually ranges in value from $0.1 < \chi < 1.0$, and conventionally is set to 0.9 [36]. The density ρ_{for}^s is the forest dislocation density, which is governed by Refs. [37,38]:

$$\frac{\partial \rho^\alpha}{\partial \gamma^\alpha} = k_1^\alpha \sqrt{\rho^\alpha} - k_2^\alpha \rho^\alpha \tag{3}$$

where k_1^α is a rate-insensitive coefficient for dislocation storage by statistical trapping of mobile dislocations, and k_2^α is the coefficient for dynamic recovery by thermally activated mechanisms.

The stress τ_{deb}^α represents the hardening contribution of dense dislocation substructures and is represented by an extended Taylor law, as inspired by the model proposed by Basinski et al. [39], given by:

$$\tau_{\mathrm{deb}}^\alpha = \mathrm{k_{deb}} \mu \mathrm{b}^\alpha \sqrt{\rho_{\mathrm{deb}}} \log\left(\frac{1}{\mathrm{b}^\alpha \sqrt{\rho_{\mathrm{deb}}}} \right) \tag{4}$$

The last term in Eq. (2), τ_{TB}^s, is the barrier effect provided by twin boundaries formed within the grain and formulated based on a Hall-Petch relationship with $d_{mfp}^{s,PTS}$:

$$\tau_{TB}^s = \mu H P^{\alpha\beta} \sqrt{\frac{b^\alpha}{d_{mfp}^{s,PTS}}} \quad s \in \alpha \;\; \text{with } \beta - \text{type} \;\; \text{PTS} \tag{5}$$

Here, $HP^{\alpha\beta}$ is a dimensionless coefficient and $d_{mfp}^{s,PTS}$ is mean free path of slip in the matrix regions between adjacent twin boundaries.

3.3. Composite grain model

To model the reorientation of the lattice by twinning, twin growth, and the directional barriers twin boundaries impose on slip, we utilize the *uncoupled twin-matrix* version of the composite grain (CG) twin model presented in Refs. [35,40,41]. To begin, every twin-free grain is tested in every increment to identify whether its volume should be divided into a representative twin domain and matrix domain. First, the shear rate for each twin variant t, $\dot{\gamma}^t$, is determined using the same flow rule as for slip, i.e.,

$$\dot{\gamma}^t = \dot{\gamma}_0 \left| \frac{m^t : \sigma}{\tau_0^\beta} \right|^n \mathrm{sign}(m^t : \sigma) \tag{6}$$

τ_0^β , corresponds to a critical value to migrate the twin boundary and grow the twin. At each time increment, the twin volume fraction, given by

$$f^t = \frac{\Delta \gamma^t}{s} \tag{7}$$

for each twin system t can be estimated, where $\Delta\gamma^t = \dot{\gamma}^t \Delta t$ is the shear contributed by the twin system t during the time increment, Δt is the increment in time, and S is the characteristic twin shear.

3.4. Twin affected dislocation storage rates

In some test orientations, the stress strain response of Mg alloys can exhibit inflections in the hardening rate, which are known as twinning signatures, signifying that twinning is occurring in addition to slip. Interactions between dislocations and growing twins have been consid-

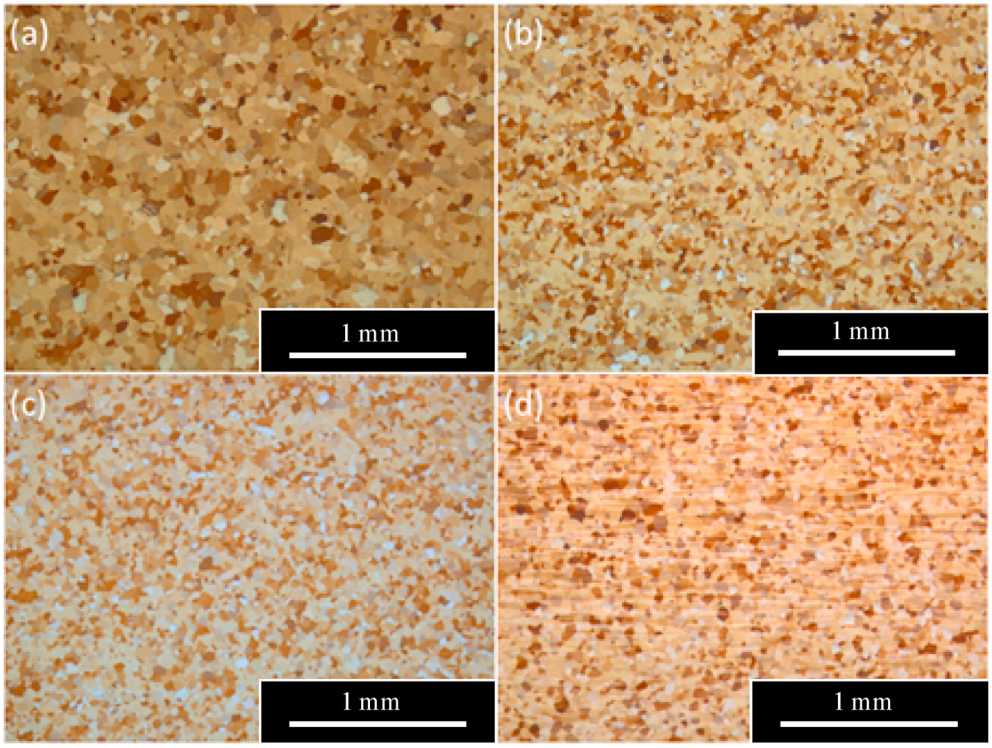

Fig. 1. Optical micrographs showing the microstructure of recrystallized Mg–Y plates: (a) Mg-0.2Y; (b) Mg-0.6Y; (c) Mg–1Y; (d) Mg–3Y. Note that the grain sizes are similar in Mg-0.6Y, Mg–1Y, and Mg–3Y, whereas Mg-0.2Y exhibits a slightly larger grain size due to the rapid grain growth in Mg with low Y content.

ered to contribute to such distinctive changes in hardening. Several possible dislocation/twin interaction scenarios have been discussed. The most common one is that the twin boundary serves as a directional barrier to slip, which can be represented by an additional resistance τ_{TB} to the CRSS for slip, as reflected in Eq. (5) [42–44]. A phenomenon called transmutation has been reported. In particular, Wang et al. preformed a TEM study on Mg alloy and found that <a>-type dislocations can be transformed into <c+a>-type dislocations by the twin [45,46]. Third, a dislocation could, instead, transmit across the twin boundary and glide on a slip plane in the twin that is crystallographically equivalent to the original slip plane in the parent [47–49]. Last, the dislocation may be absorbed by the moving twin boundary [50,51]. In recent work, Chen et al. [51], using molecular dynamics simulation, studied the interaction between an impinging dislocation and an extension twin boundary in pure Mg. They found when the Burgers vector of a dislocation (basal, prismatic and $\{10\bar{1}1\}$ <c+a> pyramidal dislocations) is not parallel to the zone axis of the twin, the twin boundary can act as a dislocation sink, in which the matrix dislocation is absorbed by the twin boundary [51].

The latter scenario suggests that dislocations can be consumed by the migrating twin boundary, leading to a reduction in the dislocation trapping rate. This reduction is different than the reduction in dislocation density due to dynamic recovery, which is a thermally activated mechanism enabled by dislocation-dislocation reactions. Here, we extend the DD model to account for the reduction in the trapping rate caused by twin growth. To reflect this interaction, the trapping rate coefficient k_1^α in Eq. (3) for a given dislocation slip α in a given grain is made to depend on the growth rate of the twin, $\frac{\partial f}{\partial t} = \frac{\dot{\gamma}}{S}$ in the same grain. When there is no twinning, the coefficient k_1^α in Eq. (3) is constant and controls the rate of dislocation trapping with respect to shear. Yet, when twins have already formed and are growing, the coefficient decreases concomitantly, resulting in a decrease in the trapping rate. To capture this effect, we adopt the following exponential decay law

$$k_1^\alpha = k_0^\alpha \exp\left(- C \sum_t \frac{\partial f^t}{\partial t} \right) \tag{8}$$

where $\frac{\partial f}{\partial t} = \frac{\dot{\gamma}}{S}$ is the twin growth rate in the CG model, $C = \frac{\dot{\gamma}_0}{S}$, where $\dot{\gamma}_0$ is a reference shear rate defined in Eq. (6), and k_0^α is the initial trapping rate coefficient in the twin-free grain.

3.5. Model set up for simulation

The inputs required in the model include the initial crystallographic texture, initial morphological texture (i.e., grain shape distribution), the applied boundary conditions, and the available slip and twinning modes. Here, we make available to the calculation the slip and twinning modes that are commonly observed in experiment: $\{0001\}11\bar{2}0$ basal slip, $\{10\bar{1}0\}1\bar{2}10$ prismatic slip, $\{10\bar{1}1\}11\bar{2}3$ pyramidal slip, and $\{10\bar{1}2\}\bar{1}011$ extension twin [1,11,23–25,52,53]. As more confirmation, TEM and EBSD analyses on the Mg–Y alloys in the present study (shown later) and an *in-situ* TEM study of a Mg-2.5 at.% Y alloy from our previous work [18] also observed dislocations from these same modes and $\{10\bar{1}2\}\bar{1}011$ type extension twins. Other twin types, such as the $\{10\bar{1}1\}$ contraction twins and $\{10\bar{1}2\} - \{1\bar{0}\bar{1}1\}$ double twins, while seen in other Mg alloys were not observed in the present experiment. This result is consistent with recent work by Ansari et al., who studied the influence of Y addition (5 wt% and 10 wt%) on the recrystallization, texture and mechanical properties of Mg–Y alloys [54]. In their work, double twins and contraction twins are found to be dominant in Mg-10 wt% Y, while only the $\{10\bar{1}2\}$ extension twin is dominant in the Mg-5 wt.% Y alloy [54]. This difference was explained by a significant decrease in the basal pole texture intensity. In our work, the Y concentration is not only lower than 5 wt%, but the texture is also stronger; therefore, it is reasonable to only consider $\{10\bar{1}2\}$ twin system in our calculations.

Each slip mode is assigned a very small initial dislocation density of $1 \times 10^{10}/m^2$, a value that has been found to not affect the evolving

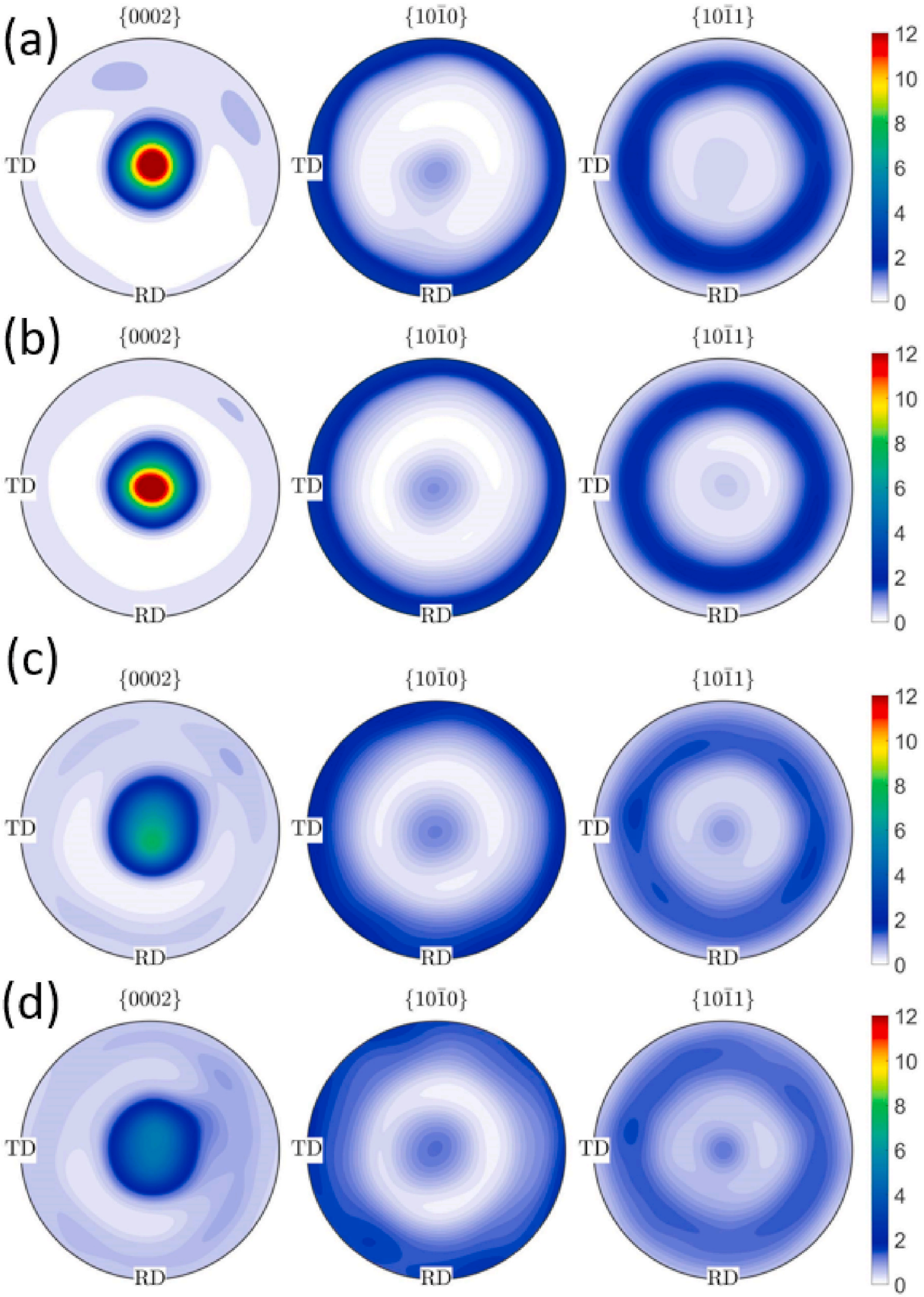

Fig. 2. Experimentally determined {10-10}, {0002} and {10–11} pole figures showing the initial rolling texture measured using XRD for: (a) Mg-0.2Y, (b) Mg-0.6Y, (c) Mg–1Y and (d) Mg–3Y.

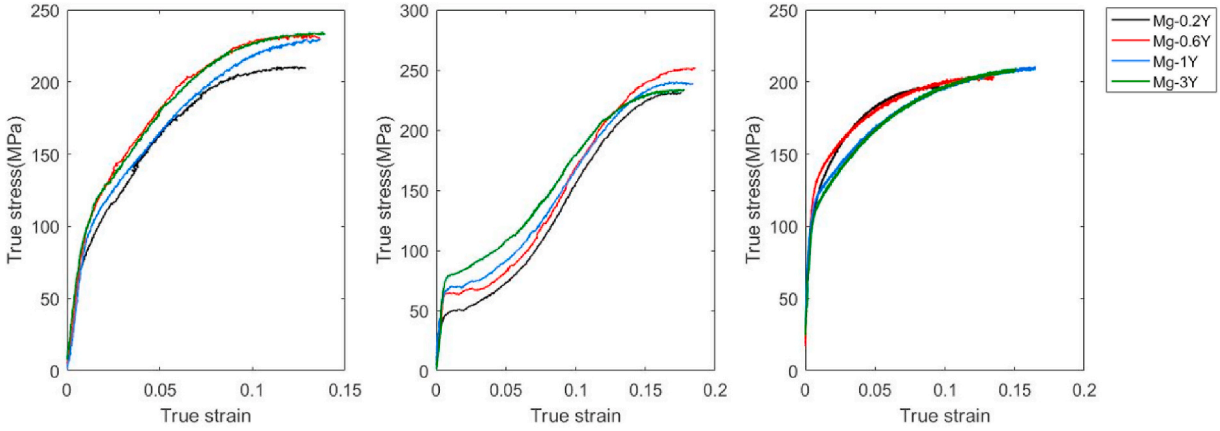

Fig. 3. Experimental stress-strain curves for the for Mg–Y alloys under: (a) normal direction compression (ND-C), (b) rolling direction compression (RD-C), and (c) rolling direction tension (RD-T).

dislocation density in prior studies [55]. For the initial texture the model material used the measured texture for each alloy, represented using 1000 weighted orientations. The initial shape for all grains is spherical, representing the nearly equiaxed structure. The mechanical tests were simulated by imposing 0.002 strain increments along the RD or ND, in the appropriate sense of loading (compression or tension), while enforcing zero average stress along the lateral two sample directions. The macroscopic strain rate is 0.001, equal to that used in the experimental tests. In simulation, the dislocation density, grain shape and texture were continuously updated. The calculated textures are plotted also using the MTEX software to compare directly with the measurement [31].

4. Results

4.1. Initial microstructures and textures

After hot rolling to the same thickness reduction and recrystallization annealing, the microstructures of the four Mg–Y alloys were characterized using optical microscopy (Fig. 1). The micrographs revealed a nearly equiaxed and twin-free microstructure with no detectable precipitates. The equilibrium solubility limit of Y in Mg at ambient temperatures is ~0.6 wt% Y. Using XRD (see Fig. A1), we find that evidence of a second phase only in the Mg–3Y alloy. The average grain sizes measured from optical microscopy are listed in Table 1. To achieve a similar average grain size in the alloys, higher annealing temperature and/or longer annealing time is needed for alloys with a higher Y concentration. It is noted that due to the rapid grain growth of Mg-0.2Y at elevated temperatures, its grain size is slightly larger compared to the other three Mg–Y alloys, despite the lowest temperature and shortest annealing time being used.

The starting textures were measured using XRD. Fig. 2 shows the {10-10}, {0002} and {10–11} pole figures of the initial textures for these four alloys. All alloys exhibit primarily basal-type rolling textures. However, a noticeable texture weakening effect with an increase in the Y concentration is observed. The maximum basal texture intensities are 21.2, 15.7, 7.3 and 5.3 multiples of uniform distribution (m.u.d.), respectively, for Mg-0.2Y, Mg-0.6Y, Mg–1Y and Mg–3Y.

4.2. Mechanical response

Quasi-static uniaxial mechanical tests along three loading directions were performed at room temperature on the four Mg–Y alloys. The stress-strain curves up to the ultimate stress are presented in Fig. 3 (a, b and c) for the ND-C, RD-C and RD-T test directions, respectively. According to the initial basal rolling texture of these alloys, in the ND-C test, the compression direction is roughly parallel to the c-axes for most of the grains, a condition which would favor pyramidal <c+a> slip. For ND-C, the 0.2% offset yield strengths ($\sigma_{0.2\%}$) are 83, 105, 97 and 101 MPa for Mg-0.2Y, Mg-0.6Y, Mg–1Y and Mg–3Y, respectively. After yielding, the hardening rate continuously decreases with increased strain, suggesting a slip-dominated response [13,56]. In contrast, in the RD-C test, the compression axis is perpendicular to the c-axes of a majority of the grains, requiring the crystals to extend along the c-axis. The stress-strain curves in this case have a sigmoidal shape, i.e., the strain hardening rate first increases and then decreases after yield, which is a typical signature for $\{10\bar{1}2\}\langle\bar{1}011\rangle$ twinning-dominated deformation. The $\sigma_{0.2\%}$ for RD-C of Mg-0.2Y, Mg-0.6Y, Mg–1Y and Mg–3Y are 46 MPa, 64 MPa, 67 MPa and 78 MPa, respectively, lower than those in the ND-C test. During RD-T, when the tension axis is perpendicular to the c-axes, activation of prismatic <a> slip would be, however, favored instead of $\{10\bar{1}2\}\langle\bar{1}011\rangle$ twinning or pyramidal <c+a> slip. The $\sigma_{0.2\%}$ values for Mg-0.2Y, Mg-0.6Y, Mg–1Y and Mg–3Y are higher than those for ND-C and much higher than those for RD-C and are 112, 126, 107 and 110 MPa, respectively. For a general view, the yield strengths as a function of loading direction and composition are plotted in Fig. 4.

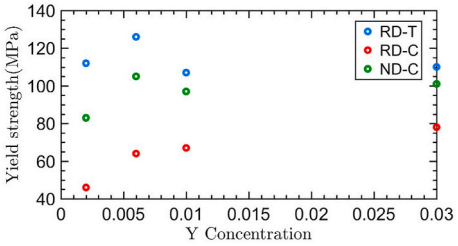

Fig. 4. Yield strength for Mg–Y in different loading directions and composition.

Several interesting findings arise from these tests. First, in ND-C and RD-T, the strains-to-failure of these Mg–Y alloys are generally higher than pure Mg. The typical strain-to-failure values in tension along the RD direction in pure Mg are below 5% [21,57], while, here, significantly enhanced strains-to-failure to more than 10% are observed, a result that has also been reported previously [17,21,57]. Second, all alloys exhibit a tension-compression (T-C) asymmetry in the RD direction, with the yield strength higher in tension than in compression. The RD tension-compression yield strength asymmetry, when quantified by $\sigma_{0.2\%}$ (RD-T)/$\sigma_{0.2\%}$ (RD-C), results in 2.4, 2.0, 1.6 and 1.4, for Mg-0.2Y, Mg-0.6Y, Mg–1Y and Mg–3Y respectively. While the values are larger than 1, they decrease with higher Y concentrations. The reduction in T-C asymmetry results from the increase in RD-C yield strengths but virtually

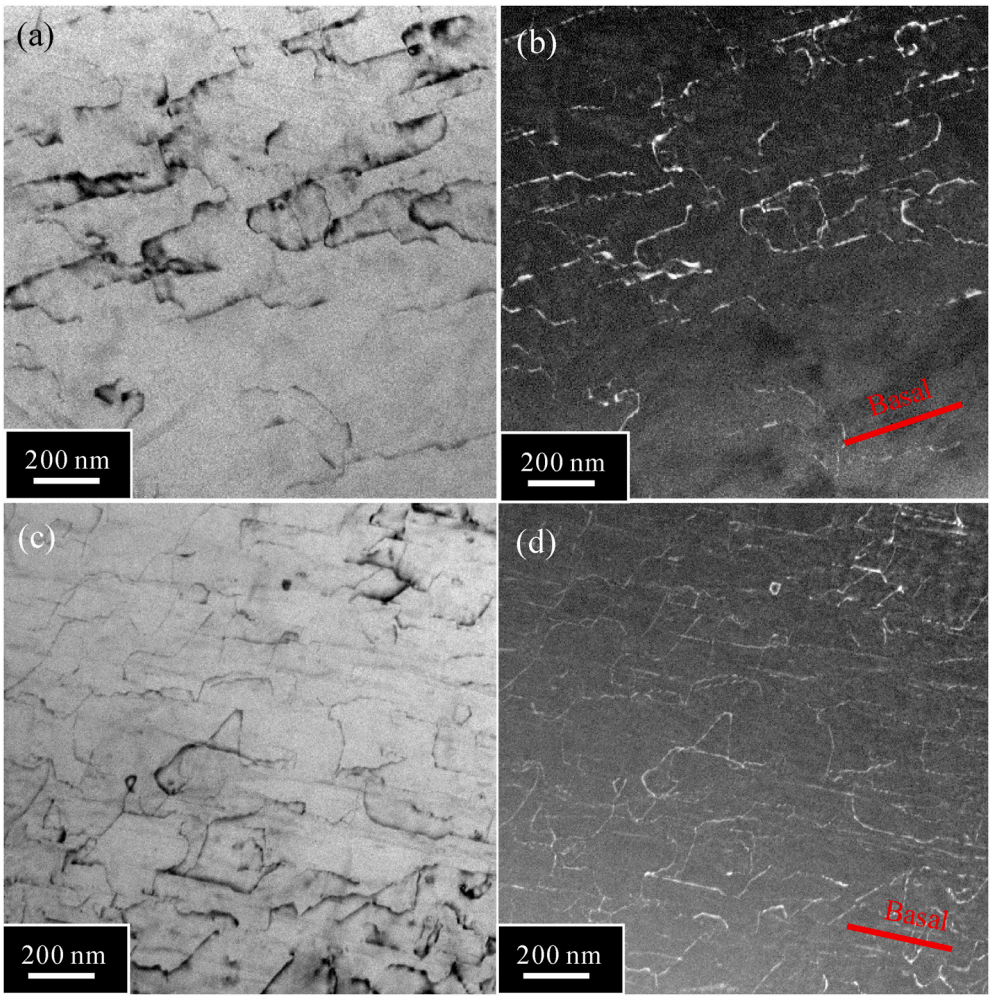

Fig. 5. Representative TEM micrograph of ~2% ND compressed Mg–1Y, at zone axes of (a, b) B = 11–20 and (c, d) B = 10-10, with diffraction vector g = [0002] showing the general activation of dislocations with <c+a> Burgers vectors.

no change in RD-T yield strengths with higher amounts of Y. Last, we observe an optimum Y-concentration of Mg-0.6Y for peak yield strength in the ND-C and RD-T tests. The same behavior is not observed in RD-C. While each load direction exhibits its own dependencies on Y, it is more important to note that the plastic anisotropy, dependence in yield strength on load direction, continuously reduces as Y increases.

4.3. Pyramidal <c+a> slip

To investigate the change in pyramidal <c+a> slip activity in Mg–Y compared to pure Mg, we performed TEM analyses on the deformed microstructure of the ND-C material. Fig. 5 shows typical two-beam bright and dark field TEM images of ND-C deformed Mg–1Y at grains with c-axes close to the compression axis. The diffraction vector g = 0002 was used to identify the presence of dislocations with non-basal Burgers vectors (<c> type dislocations). A uniform distribution of <c> type dislocations is observed, with many of them lying partially along the basal plane trace and partially out of the basal plane. Fig. 6 shows, for comparison, a TEM image of the ND-C deformed pure Mg to the same strain. Overall, the density of <c> type dislocations is lower than in Mg–Y. Also, the <c> type dislocations are localized at regions corresponding to stress concentrations, such as grain boundaries, twin boundaries or slip bands. Fig. 6 shows a band of <c> type dislocations that are found in front of a twin tip located at the top left corner of the micrographs. The non-uniform distributions of <c> type dislocations existing only close to stress concentrators in pure Mg in contrast to the uniformly distributed <c> type dislocations in Mg–1Y suggests that their activation is more difficult in pure Mg and requires a higher local stress than Mg–1Y.

4.4. Simulations of Y-affected deformation response

The observed effects of Y concentration on stress-strain response and T-C asymmetry could be due to a number of factors. They may be attributed to texture weakening and/or changes in the resistances for the slip and twinning modes as Y changes. Y concentrations are found here to affect the initial texture, weakening it as Y increases, a factor that could also contribute to lower T-C asymmetry. As shown in Fig. 2, the initial textures for these four Mg–Y alloys are relatively strong with the majority of grains with their c-axes oriented through the ND of the rolled sheet. In polycrystals, each grain by virtue of their different orientations will have different slip activities, involving multiple active slip systems and twin evolution. In addition, the reason for lower T-C asymmetry can also be attributed to the strengthening effect on each deformation mode due to Y alloying. A third factor concerns the interplay between slip, twinning, and texture evolution. When deformed under an applied strain, the texture changes, and thus, the relative activities of the different slip and twinning modes could change with strain as well. Thus, many factors are at play, which can complicate identifying how Y concentration impacts stress-strain response. To transcend the effects of texture and pointedly connect the stress-strain response of Mg–Y alloys to the activation of the various slip and twinning modes, VPSC

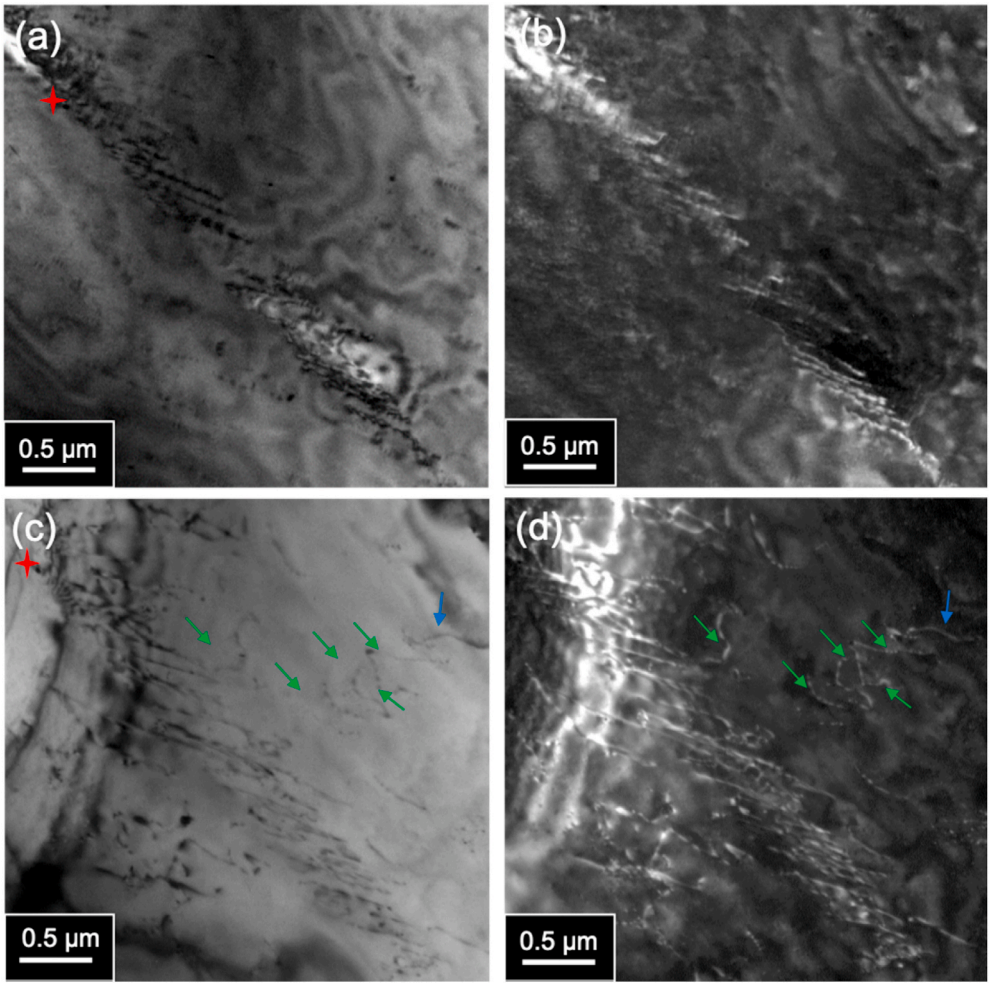

Fig. 6. A slip band of <c+a> dislocations in front of a twin tip in pure Mg with (a, b) g = [0002] and some <a> dislocations are seen with (c, d) g = [10–10]. Green arrows mark the <a> dislocations out of the basal plane, and blue arrows mark the basal <a> dislocations. The red star points at a fiduciary mark just to guide the eye. (For interpretation of the references to color in this figure legend, the reader is referred to the Web version of this article.)

polycrystal modeling was employed. All three distinct loading paths, RD-C, RD-T, and ND-C, and for four binary Mg–Y alloys were simulated.

One of the main results from this work is the identification of a single set of material-related hardening parameters that enabled the simulation to replicate all three stress-strain curves for each alloy Y concentration: Mg-0.2Y, Mg-0.6Y, Mg–1Y and Mg–3Y. Figs. 7–9 compare the calculated true stress-strain response with the measured stress-strain response. The model captures reasonably well the evolution in stress and hardening rates in all tests. Some slight deviations are noted, for instance in the Mg-0.6Y curve for RD-T. Although the flow stress is a little overestimated in this one case, the strain hardening is accurately captured. The corresponding parameter sets are given in Table 2 for the four Mg–Y alloys. Other predictions from the model are slip mode activity and evolution of texture and twin volume fraction with strain, which are discussed in turn below.

5. Discussion

5.1. Influence of Y concentration on initial critical activation stresses for slip and twinning

Fig. 10 shows the variation in τ_0^α and τ_0^β with Y concentration for each slip and twinning mode. Basal slip remains the easiest deformation mechanism for the binary Mg–Y alloy, a result that is consistent with many previous works on Mg and Mg alloys [11,52,53]. The non-basal slip modes are substantially larger than that for basal slip. The initial resistance for basal slip exhibits a proportional dependency on Y concentration, increasing with increasing amounts of Y concentration. The τ_0^α for prismatic slip and for twinning, however, are notably less sensitive to Y concentration. For comparison, similar models have reported lower τ_0^α values of 3 MPa, 36 MPa, and 86 MPa for basal, prismatic, and pyramidal slip for pure Mg [58]. A few studies have focused on the effect of Y on CRSS values, with results that are not consistent with those reported here. Stanford et al. [59] investigated the CRSS values for various deformation modes in Mg-0.5 wt% Y and Mg-2.2 wt% Y using the elasto-plastic self-consistent method. They found that for this composition range, no additional hardening on basal slip and extension twinning were observed. They state that this observation implies that the solute strengthening of these deformation modes is exhausted when concentrations reach 0.5 wt% Y. The results here, however, suggest that there is a strengthening effect on these two deformation modes, although it is small. We also observe a strengthening effect on first-order pyramidal slip, in agreement with a few studies [24,60], but not one on prismatic slip. Kula et al. [60] studied Mg–Y binary alloys with Y concentrations ranging from 1 wt% to 4 wt%. In the range 1 wt% to 3 wt%, they also found little change in the CRSS values for prismatic slip (less than 5 MPa), consistent with our finding. They only observed large changes in CRSS from 3 wt% to 4 wt%. It should be noted that the τ_0^α analyzed here only represents the initial CRSS value, and in our model the CRSS can rise from τ_0^α as strain evolves. Arguably, more important than absolute

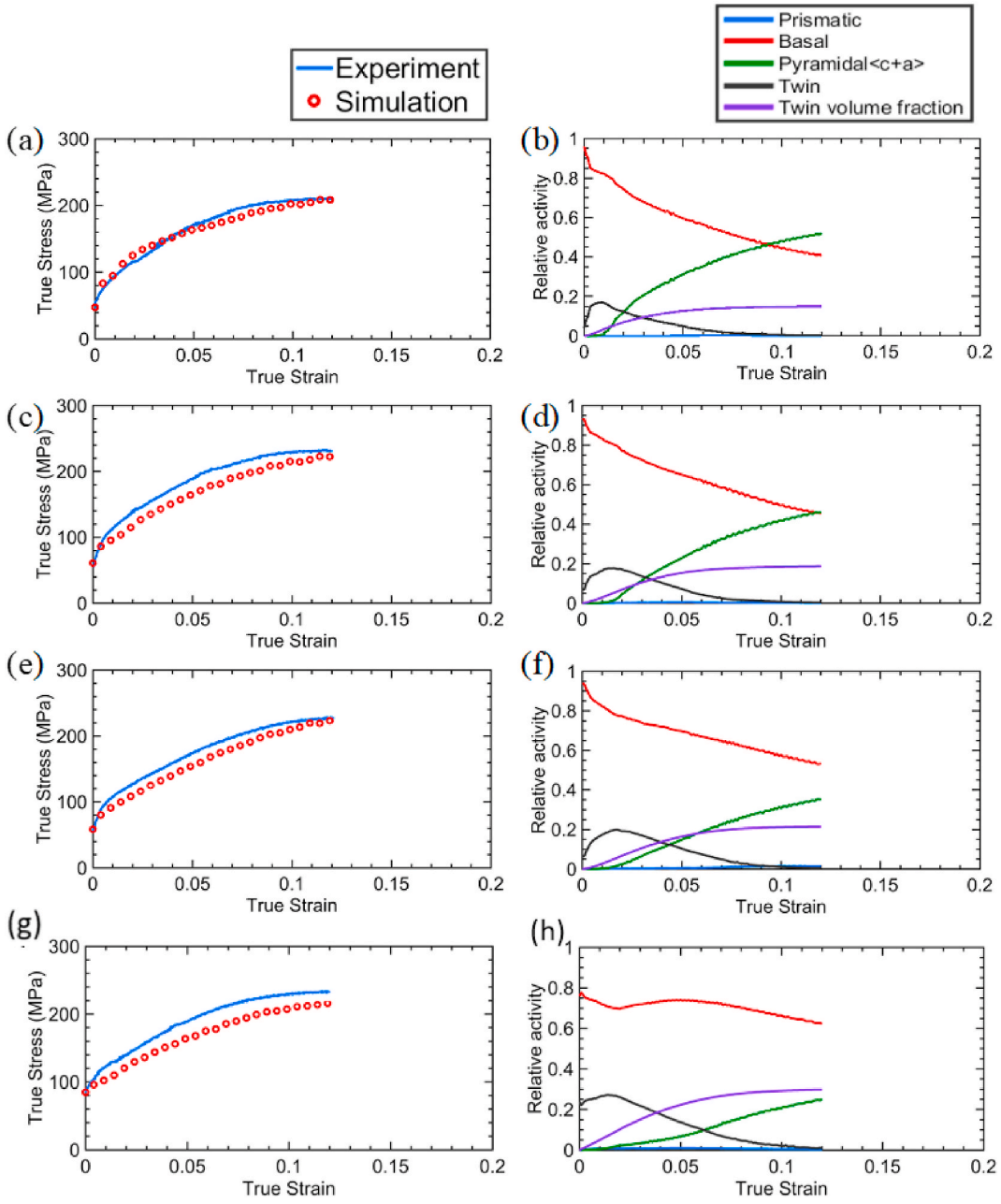

Fig. 7. Experimental and simulated stress-strain curves for ND-C for: (a) Mg-0.2Y, (c) Mg-0.6Y, (e) Mg–1Y and (g) Mg–3Y; and the corresponding plots of the relative activity of multiple slip and twinning modes for: (b) Mg-0.2Y, (d) Mg-0.6Y, (f) Mg–1Y and (h) Mg–3Y, respectively.

CRSS values are the change in the CRSS (non-basal)/CRSS (basal) ratio with increasing amounts of Y. Here we show that τ_0^{α} for basal slip increases faster compared with the non-basal slip, resulting in the reduction in this ratio as Y concentration increases.

5.2. *Y-dependent slip and twinning activity in Mg–Y alloys*

From the polycrystal model calculations, the polycrystal average amounts of slip and twinning contributed by each mode can be extracted. The columns on the right-hand side of Figs. 7–9 present the calculated relative activities (RA^{α}) of basal slip, prismatic slip, and pyramidal <c+a> slip and activities of $\{10\bar{1}2\}\bar{1}011$ extension twinning during strain evolution. We first notice that the relative slip activity for basal slip dominates in all Y concentrations and in all loading directions. The amount and type of secondary slip, as well as the participation of twinning, is, however, highly dependent on the loading direction and Y concentration.

From Fig. 6, for the four Mg–Y alloys being investigated, the hardening rate in the flow stress-strain response in ND-C decays with strain, indicating that their deformation is dominated by slip. In agreement, the VPSC calculation indicates that the response was enabled by the activation of slip and little twinning. Deformation twinning occurs only in the early stages and reduces in activity with increased ND-C strain. For the full range of Y, the twin volume fraction saturates to 15%–20% at a strain level around 8%. As mentioned, basal slip dominates, but, apart from basal slip, pyramidal <c+a> slip is the secondary slip mode, while prismatic slip activity is negligible. With ND-C straining, the contribution of pyramidal <c+a> slip increases, while that for basal slip decreases. With increasing Y concentration, the relative contribution of pyramidal <c+a> slip with respect to basal slip decreases. This reduction in <c+a> contribution causes the reduced hardening rate observed with higher concentrations of Y during ND-C.

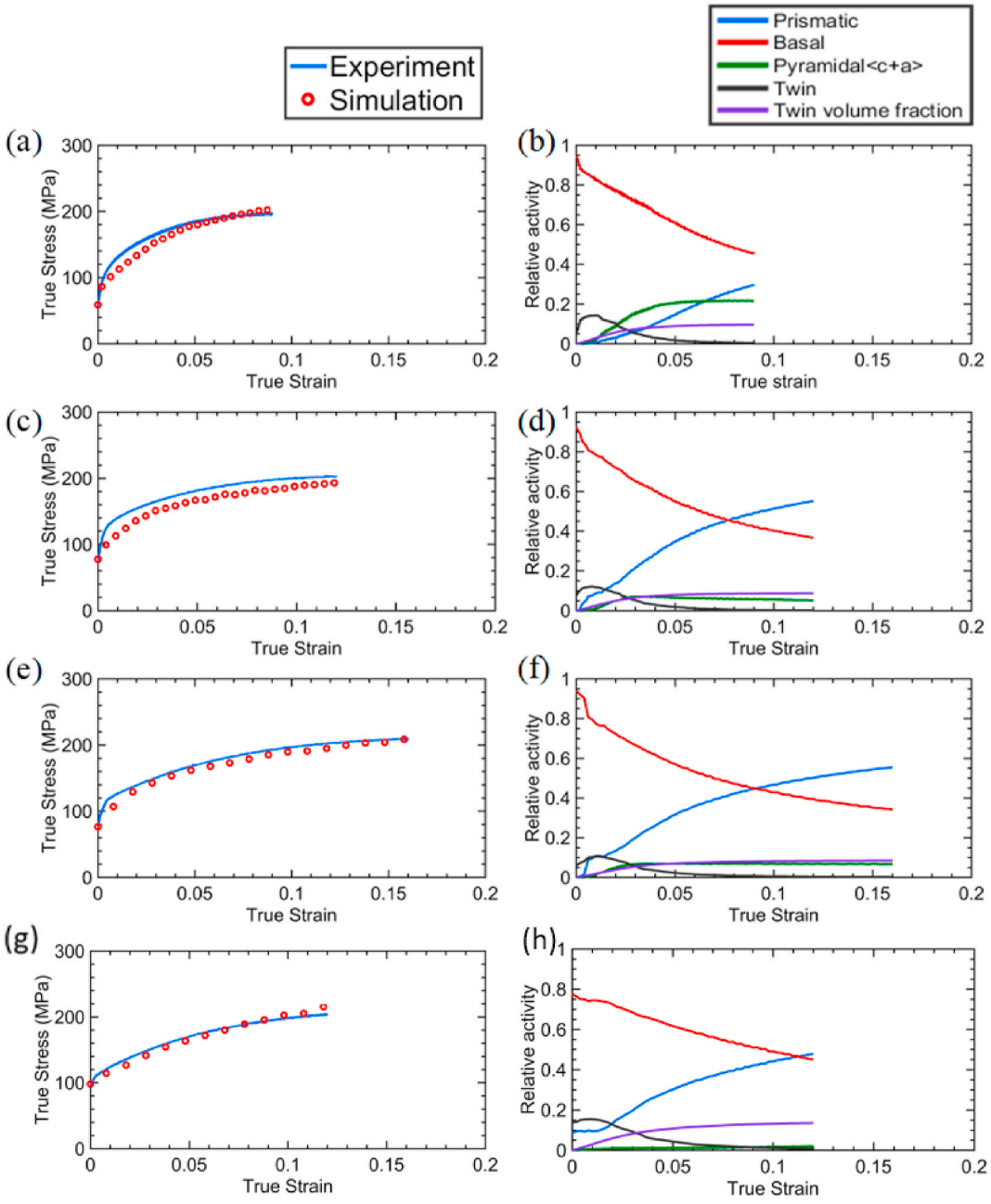

Fig. 8. Experimental and simulated stress-strain curves for RD-T for: (a) Mg-0.2Y, (c) Mg-0.6Y, (e) Mg–1Y and (g) Mg–3Y; and the corresponding plots of the relative activity of multiple slip and twinning modes for: (b) Mg-0.2Y, (d) Mg-0.6Y, (f) Mg–1Y and (h) Mg–3Y, respectively.

Like in ND-C, the hardening rate decreases with strain in RD-T (Fig. 8), suggesting also slip-dominated plasticity. In accord, the calculations of the slip and twinning activities indicate that the primary slip mode is basal slip, while the secondary slip mode is prismatic slip. Compared to the other two loading directions, deformation twinning contributes the least in RD-T. For all four Y concentrations, the relative contribution of prismatic slip rises with increased strain. As Y concentration increases from Mg-0.2Y to Mg–1Y, the contribution of prismatic slip increases. But for Mg–3Y, the relative activity of prismatic slip reduces below that in Mg-0.6Y and Mg–1Y. The predicted τ_0^{α} value for prismatic slip is insensitive to Y, being especially similar in Mg–3Y, Mg–1Y and Mg-0.6Y. Therefore, the lower activity of prismatic slip in the RD-T test for Mg–3Y can be attributed to its weaker initial texture.

Distinct from the other two loading directions, the flow stress-plastic strain response for RD-C exhibits a sigmoidal shape, a typical signature for twinning-dominant deformation behavior. The calculations predict that basal slip and twinning are the more active modes for the entire straining period, with pyramidal slip activity substantially lower and prismatic slip virtually inactive. In this test, twinning directly competes with and evidently, is favored over pyramidal <c+a> slip. With further straining (>5%), the twinning rate starts to decrease, and non-basal slip becomes active, although still in small amounts. Table 3 compares the calculated strains at which twinning activity reduces and non-basal slip activity initiates. As shown, as Y increases, the strain at which twinning activity reduces and non-basal slip activity initiates decreases. When the maximum flow stress is reached, the calculated twin volume fraction is substantial, lying within a range of 40–60% (Fig. 9). The relatively activities among the slip and twinning modes are similar for all Y concentrations. There is slightly less twinning activity and twin volume fraction at a given strain for greater Y concentrations.

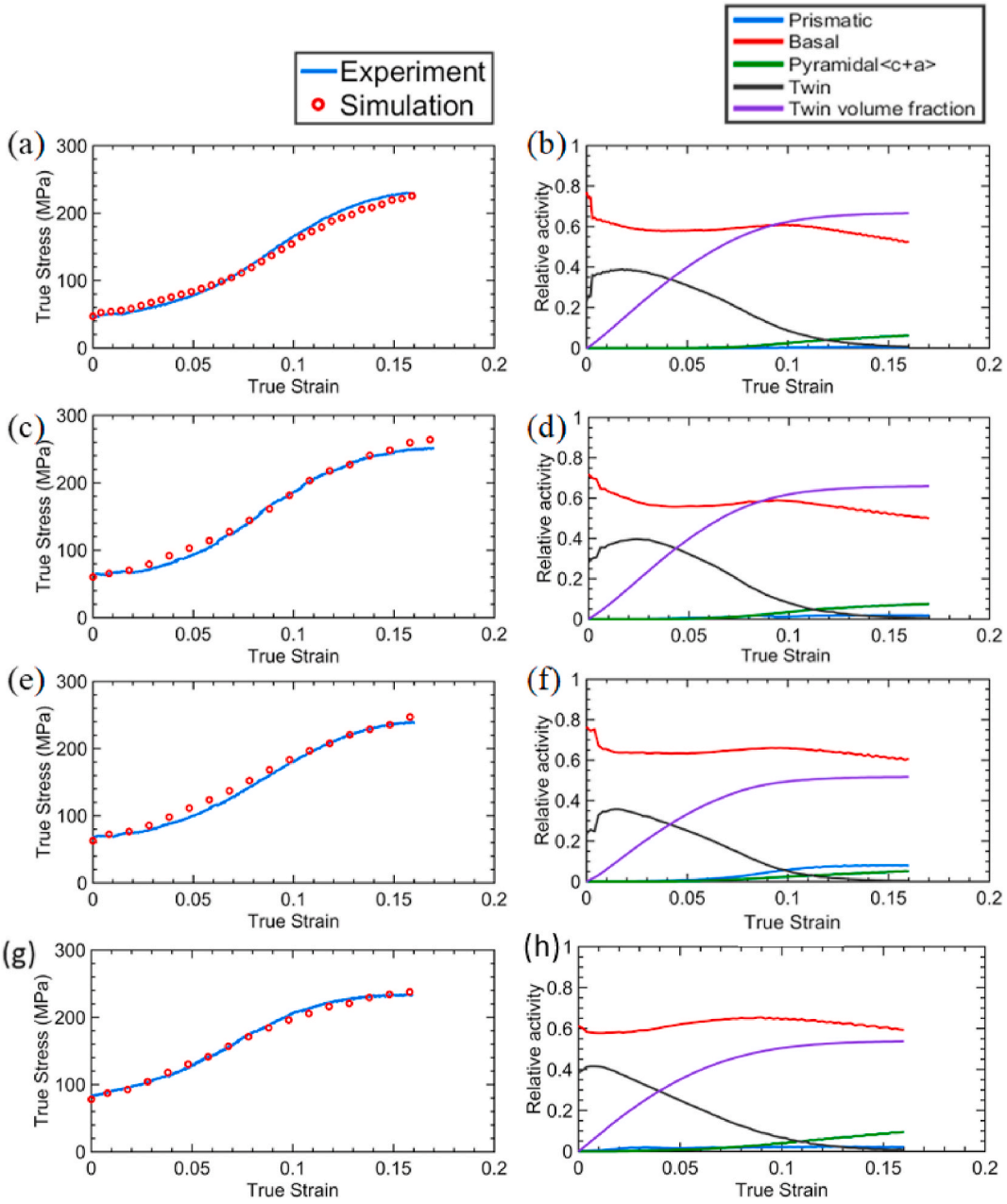

Fig. 9. Experimental and simulated stress-strain curves for RD-C for: (a) Mg-0.2Y, (c) Mg-0.6Y, (e) Mg–1Y and (g) Mg–3Y; and the corresponding plots of the relative activity of multiple slip and twinning modes for: (b) Mg-0.2Y, (d) Mg-0.6Y, (f) Mg–1Y and (h) Mg–3Y, respectively.

5.3. *Effect of Y on twinning*

Twin fractions can be detected post-mortem indirectly via texture analyses and directly with EBSD. Fig. 11 compares the XRD measured and VPSC simulated pole figures for Mg-0.2Y at the as-annealed state and after 5%, 7% and 13% RD-C deformation and after 10% ND-C. The measurement shows that the initial texture of Mg-0.2Y has a basal rolling texture, with strong basal pole intensity at the ND. The representation of the initial texture used in the model is evidently reasonable. In the RD-C test, the basal pole intensity at ND decreases, while the intensity at RD increases, corresponding to a ~90° rotation of the grain orientation. The formation of $\{10\bar{1}2\}\langle\bar{1}011\rangle$ twins, which reorient the crystal by ~86.3°, is one of the major causes of the abrupt change in the basal texture during RD-C. Up to a strain level of 7%, corresponding to the maximum strain hardening rate, the basal pole intensity grows stronger around RD rather than ND, as seen from both the experimental and simulation results. This change in texture indicates that the twin volume fraction has increased and potentially consumed the majority of the grains. When the RD-C strain increased to 13%, the basal pole density at RD has further intensified, suggesting that nearly all the crystals have been reoriented by $\{10\bar{1}2\}\langle\bar{1}011\rangle$ twinning.

Upon ND-C deformation, the measured and calculation textures show no substantial evolution. The deformation texture of Mg-0.2Y after 10% ND-C is similar to its initial basal texture, but with slightly higher basal pole intensity at ND. Although the model has predicted a twin volume fraction of 15% (Fig. 7d), the amount of reorientation is not sufficient to alter the bulk texture since the twins in the present case manifest as fine lamella. It has also been shown in several previous works that twin fractions need to exceed about 20% to manifest in bulk textures [55,61,62].

To examine the effect of Y concentration on texture evolution, Fig. 12 presents the experimental and simulated deformation textures for Mg-

Table 2
Parameters used for VPSC modeling for Mg–Y alloys. Superscript α refers to the slip mode (α = 1, 2, 3) and superscript β refers to the twin mode. The definitions of the parameters are provided in the text.

	Alloy	τ_0^α (MPa)	k_0^α (m^{-1})	D (MPa)	g	Q	$HP^{\alpha 1}$	C
Basal ($\alpha = 1$)	Mg-0.2Y	6	2.5 x 10^9	500	0.003	12	0	1000
	Mg-0.6Y	9	1.5 x 10^9	500	0.003	20	30	1000
	Mg-1Y	11	1.5 x 10^9	800	0.003	20	0	1000
	Mg-3Y	22	1.5 x 10^9	1000	0.002	5	100	1000
Prismatic ($\alpha = 2$)	Mg-0.2Y	105	4 x 10^9	6000	0.002	0	500	1000
	Mg-0.6Y	85	4 x 10^9	6000	0.002	0	500	1000
	Mg-1Y	85	4 x 10^9	6000	0.002	0	100	1000
	Mg-3Y	85	4 x 10^9	6000	0.002	5	500	1000
Pyramidal 2nd <a+c> ($\alpha = 3$)	Mg-0.2Y	90	5 x 10^8	2000	0.002	0	500	1000
	Mg-0.6Y	100	4 x 10^9	6000	0.002	0	500	1000
	Mg-1Y	100	6 x 10^8	2000	0.002	0	500	1000
	Mg-3Y	110	6 x 10^9	2000	0.002	0	500	1000
		τ_0^β (MPa)						
Extension Twin ($\beta = 1$)	Mg-0.2Y	10						
	Mg-0.6Y	10						
	Mg-1Y	13						
	Mg-3Y	13						

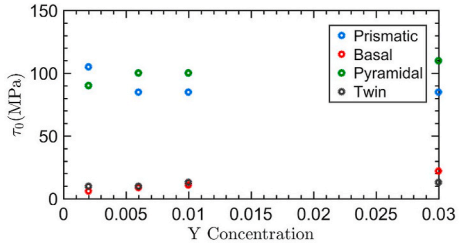

Fig. 10. Predicted initial resistances for various slip and twinning modes in Mg–Y as a function of Y concentration.

0.2Y, Mg-0.6Y, Mg–1Y and Mg–3Y at the same strain, 5% RD-C. For all Mg–Y alloys, there is a ~90° reorientation of grains after RD-C that lead to increased intensities around RD in the basal pole figures. With an increased amount of Y, the intensities in basal pole figures

Table 3
The critical strain at which twinning activity reduces and non-basal slip activity initiates decreases.

	Mg-0.2Y	Mg-0.6Y	Mg–1Y	Mg–3Y
Twinning activity reduce	0.023	0.026	0.016	0.008
Non-basal slip activity initiates	0.074	0.062	0.058	0.024

corresponding to $\{10\bar{1}2\}\langle\bar{1}011\rangle$ twinning decreased. Both modeling and measurements confirm the slip and twinning activity predictions stated earlier–increased Y content reduces slightly the propensity of but does not shut off twinning.

As an explicit way to identify Y concentration effects on twinning, the twin area fraction was measured using an EBSD-based statistical study for the four Mg–Y alloys when loaded in uniaxial RD-C condition to 5% true strain. Representative EBSD maps for 5% RD-C deformed Mg-0.2Y, Mg-0.6Y, Mg–1Y and Mg–3Y are shown in Fig. 13(a–d), showing

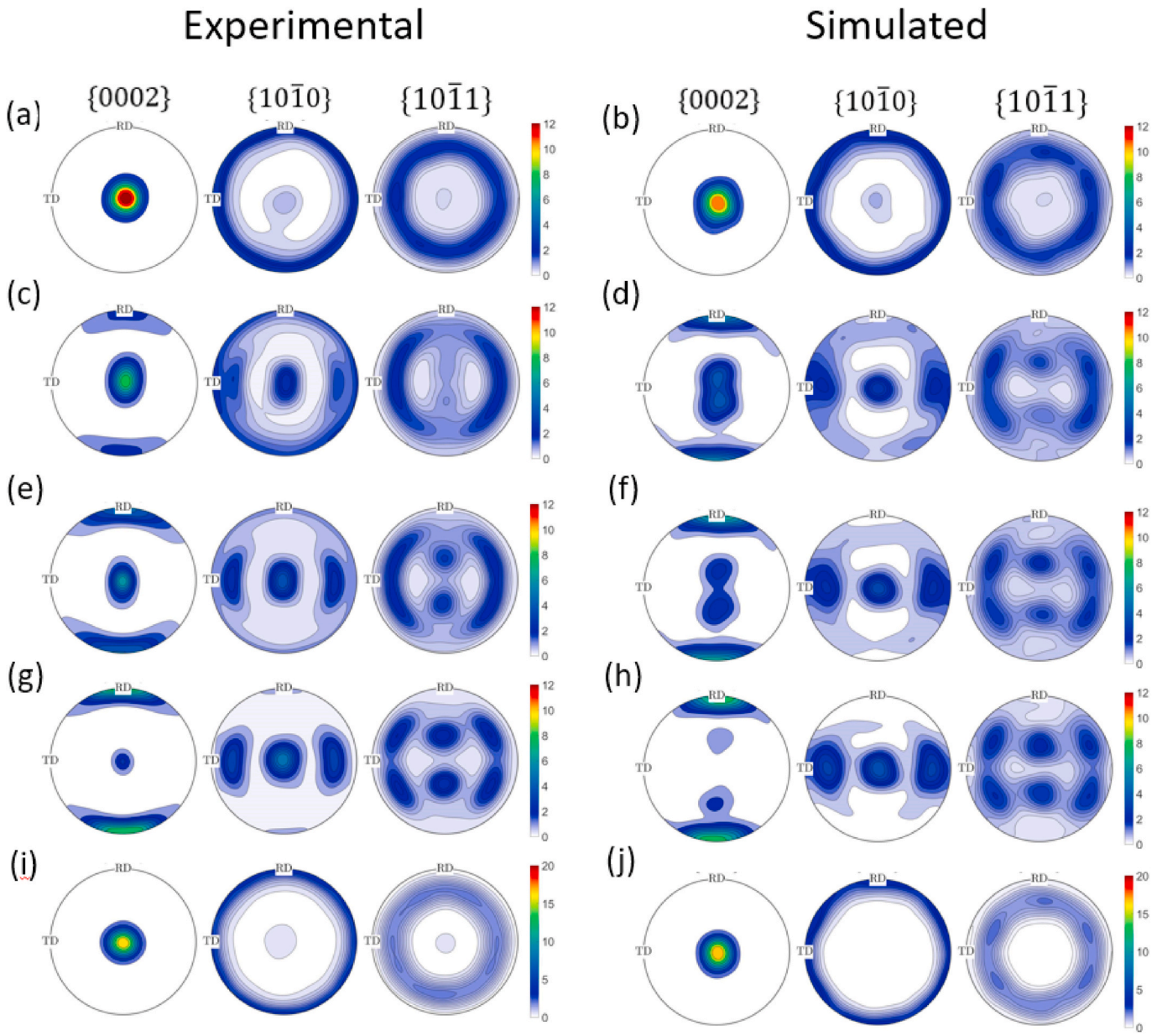

Fig. 11. Experimental and simulated pole figures showing the texture evolution in Mg-0.2Y alloys: (a, b) initial, (c, d) 5% RD-C, (e, f) 7% RD-C, (g, h) 13% RD-C and (i, j) 10% ND-C.

that all the samples contain profuse lenticular-shaped deformation twins. A careful statistical analysis was performed to quantify the twin fractions. In all samples, most of the twins are $\{10\bar{1}2\}\langle\bar{1}011\rangle$ twins, and the fraction of $\{10\bar{1}2\}\langle\bar{1}011\rangle$ twin type is negligible. Table 4 compares the area fractions of $\{10\bar{1}2\}\langle\bar{1}011\rangle$ twins measured by EBSD in the four alloys, with the values being 39%, 36%, 33% and 25% for Mg-0.2Y, Mg-0.6Y, Mg–1Y and Mg–3Y, respectively. Similar EBSD statistical analysis of extension twins in pure Mg show that the twin area fraction is about 60% for grains with a diameter of approximately 25 μm at 3% true strain [58]. Comparisons with the findings here suggests that Y addition suppresses the twin activity. VPSC calculations predicted both the relative activity of deformation twinning (Fig. 9) and the twin volume fractions (Table 4 and Fig. 14). The volume fraction of calculated by VPSC agree well with the EBSD results on twin area fractions.

The relatively low propagation stresses for extension twinning, especially compared to those for prismatic and pyramidal slip, suggest that generally twinning remains an easily activated deformation mechanism in Mg–Y alloys. With an increase in Y concentration from 0.2 to 3 wt%, the twin propagation stress slightly increases. The slightly increased propagation stress, in combination with the texture weakening with higher Y concentrations, can explain the lower fraction of twins in RD-C deformed Mg–Y and the reduced tension-compression yield asymmetry with a higher Y concentration.

5.4. *Effect of Y on plastic anisotropy and slip-twin interactions*

All four alloys exhibited similar plastic anisotropy despite the large changes in Y additions. Regarding rank, the yield stress is highest in RD-T, second in ND-C, and the lowest in RD-C. Thus, all four of the Mg–Y alloys show a RD T-C yield asymmetry greater than 1. The initial hardening rate are highest in ND-C for every alloy. However, Y concentrations affect the differences in the yield stress, among the different test directions. In this way, increases in Y additions lower the orientation dependent yield stress. The reduction can be attributed to a clear

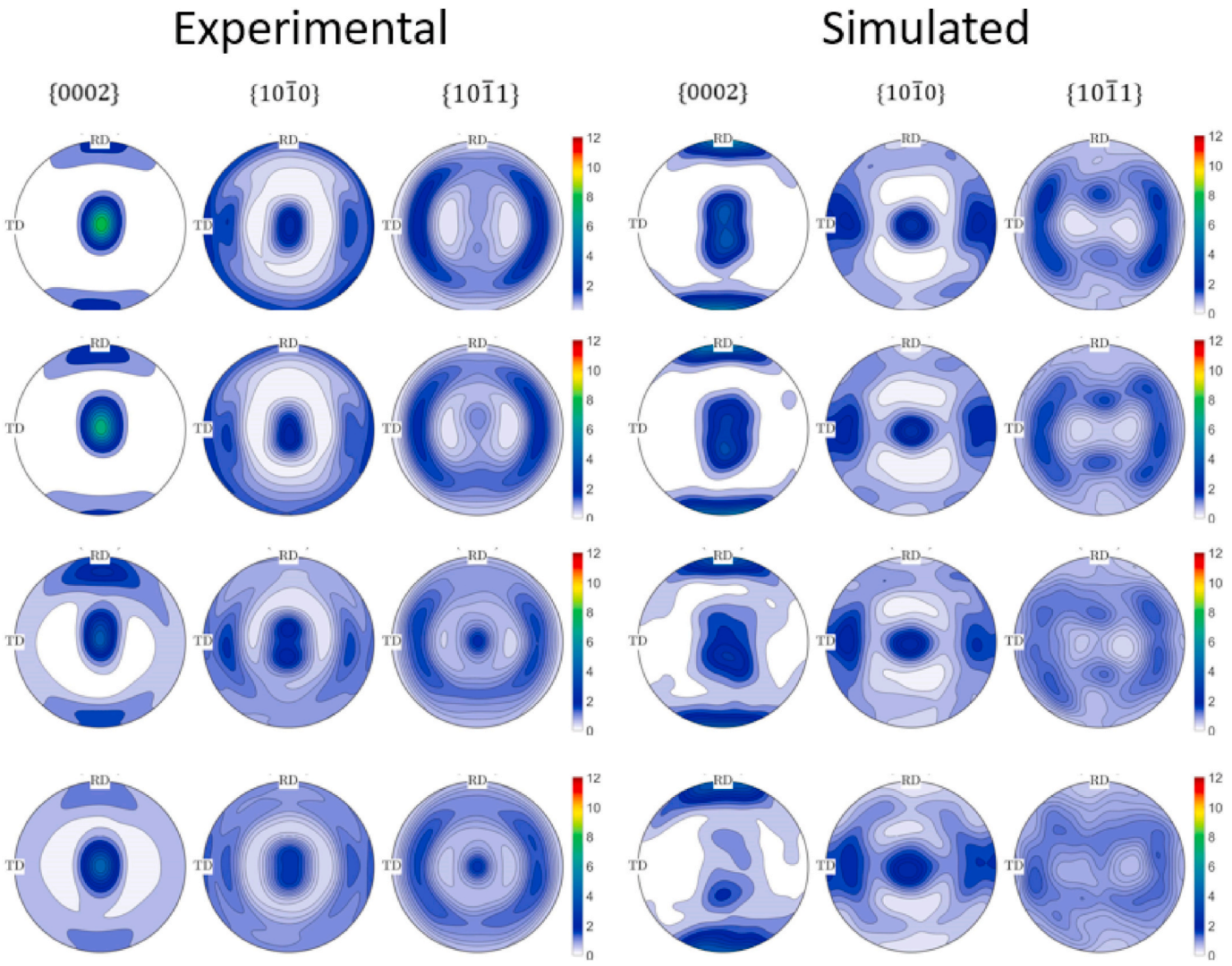

Fig. 12. Experimental and simulated pole figures of 5% RD-C deformed Mg–Y alloys: (a, b) Mg-0.2Y, (c, d) Mg-0.6Y, (e, f) Mg–1Y and (g, h) Mg–3Y.

increase in the RD-C yield stress with increase in Y, since the changes in ND-C and RD-T yield stresses are not proportional or as pronounced. While the model predicts a reduced non-basal to basal initial CRSS ratio with increased Y, this ratio may not be the main reason for the reduced anisotropy. We find that in ND-C, the contributions of pyramidal slip to deformation is important for all Mg–Y alloys but it tend to decrease slightly as Y increases. In RD-C, the twin volume fraction decreases with increasing Y and the pyramidal slip activity is slightly increased. Only in the RD-T tests does the contribution of prismatic slip increase as Y increases from 0.2% to 1%. The activity of prismatic slip in the other two directions is relatively low. In fact, basal slip dominates in all loading directions and in all alloys and the non-basal contribution does not necessarily increase as Y increases. Other factors, such as initial texture, unidirectional activation of twinning, and loading direction, can also play a role. In Mg, the pyramidal-to-prismatic initial CRSS ratio can range from 2 to 5, while current study shows that this ratio in Mg–Y is small. The reduction in CRSS ratios with Y could be a reason for the reduced anisotropy.

The modeling suggests a number of interesting slip-twin interactions. First, the absorption rate coefficient C in Eq. (8) for basal, prismatic and pyramidal slip were the same in all cases. This finding suggests a possible that Y solutes at the twin boundaries does not affect the interactions between dislocations and the twin boundary. Clearly, the growth and saturation of twinning is affected by Y as the twin volume fraction decreases with increasing amounts of Y additions. Second, the twin-barrier factor $HP^{\alpha\beta}$ for pyramidal slip is found to be 500 with all four Y concentrations, which is much larger than the factor for other two slip modes (basal and prismatic slip). This suggests that the twin boundary serves as a stronger obstacle to pyramidal <c+a> slip than the other slip modes. This effect is responsible for the rapid increase in hardening rate during the RD-C test.

6. Conclusions

A combination of microstructural characterization, texture analysis, and visco-plastic self-consistent (VPSC) modeling was employed to investigate the alloying effects of different concentrations of Y on the deformation response in Mg. In the experiment, four Mg–Y alloys were deformed along three different loading paths, tension and compression in the rolling direction (RD-T and RD-C), and compression in the normal direction (ND-C). In the model, the formulation was extended to account for the absorption of lattice dislocations as the twin boundary migrates. For each alloy, the model identified a single set of material parameters that successfully reproduced all measured stress-strain curves and achieved agreement with measured deformation textures and twin area fractions. The following conclusions on the effects of Y alloy concentrations are made:

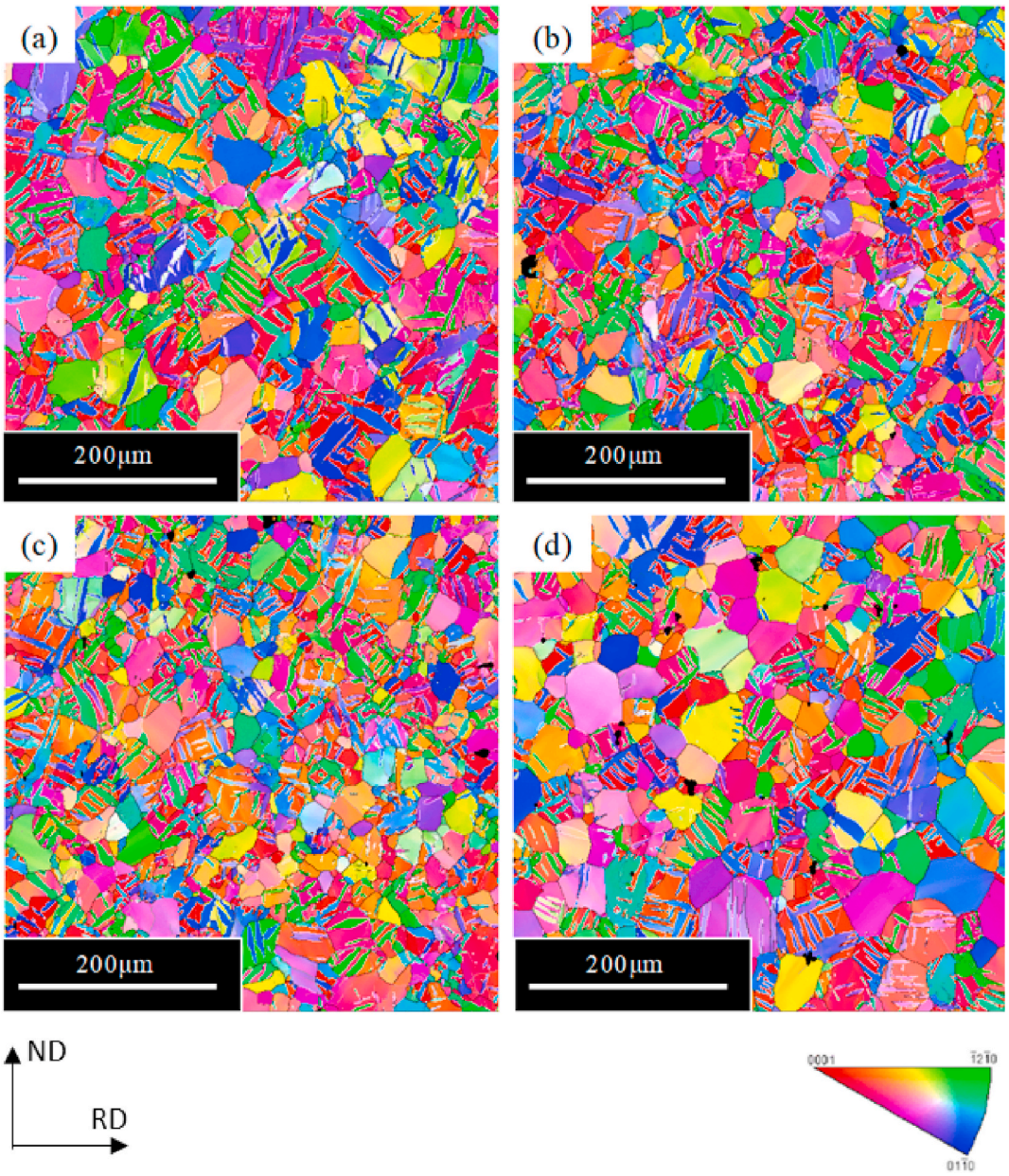

Fig. 13. Representative EBSD inverse pole figure colored maps for 5% RD-C deformed Mg–Y alloys: (a) Mg-0.2Y, (b) Mg-0.6Y, (c) Mg–1Y and (d) Mg–3Y.

Table 4
Fraction of $\{10\bar{1}2\}\langle 10\bar{1}\bar{1}\rangle$ twins after ~5% true strain compression in the rolling direction (RD-C).

	Mg-0.2Y	Mg-0.6Y	Mg–1Y	Mg–3Y
Twin area fraction by EBSD	39%	36%	33%	25%
Twin volume fraction by VPSC calculations	34.1%	32.2%	28.6%	30.1%

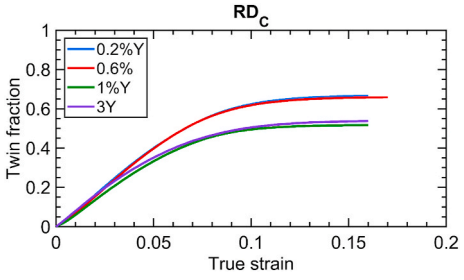

Fig. 14. Calculated twin volume fractions as a function of RD compressive plastic strain.

1. With increased Y concentration, the intensity of the initial basal rolling texture and plastic anisotropy reduce.
2. The effect of Y on yield strength, hardening rate, flow stress is not consistent among the different loading paths. Yield strength increases with Y concentration only in the RD-C test.
3. The calculations show that the initial CRSS(non-basal)/CRSS(basal) ratio decreases with increased amounts of Y due to an increase in the CRSS for basal slip but relatively little change in the CRSS for pyramidal and prismatic slip with higher concentrations of Y.
4. Despite the lower CRSS(non-basal)/CRSS(basal) ratio, more substantial contributions of <c+a> slip and the reduced plastic

anisotropy of Mg–Y alloys compared to pure Mg can be attributed to similar initial CRSS values between prismatic slip and pyramidal slip.
5. Increased Y concentration reduces the activity of $\{10\bar{1}2\}\bar{1}011$ twinning in RD-C.
6. The calculations suggest that migrating twin boundaries in Mg–Y with different concentrations have the same dislocation absorption rate.

Data availability

The raw data required to reproduce these findings are available to download from https://www.uc-twinmesh.ucsb.edu/#. The processed data required to reproduce these findings are available to download from https://www.uc-twinmesh.ucsb.edu/#

CRediT authorship contribution statement

Jiaxiang Wang: Software, Methodology, Writing – original draft. **Xin Wang:** Investigation, Resources, Writing – original draft. **Kehang Yu:** Formal analysis. **Timothy J. Rupert:** Writing – review & editing, Conceptualization. **Subhash Mahajan:** Writing – review & editing, Conceptualization. **Enrique J. Lavernia:** Writing – review & editing, Conceptualization. **Julie M. Schoenung:** Writing – review & editing, Conceptualization. **Irene J. Beyerlein:** Writing – review & editing, Supervision, Funding acquisition, Project administration.

Declaration of competing interest

The authors declare that they have no known competing financial interests or personal relationships that could have appeared to influence the work reported in this paper.

Acknowledgements

The authors would like to thank Dr. Sangbong Yi and his colleagues at HZG for providing the Mg–Y materials for this study. The authors acknowledge financial support from the National Science Foundation (NSF) CMMI-1729887 (UCSB), CMMI-1729829 (UCI), and CMMI-1723539 (UC Davis).

Appendix

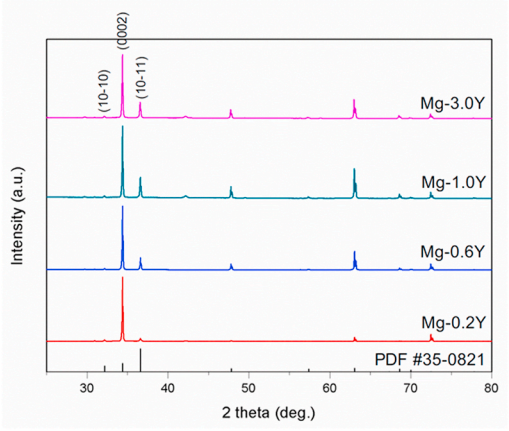

Fig. A1. X-ray diffraction data for Mg–3Y.

References

[1] S.R. Agnew, Ö. Duygulu, Int. J. Plast. 21 (2005) 1161–1193.
[2] E.A. Ball, P.B. Prangnell, Scripta Metall. Mater. 31 (1994) 111–116.
[3] M.R. Barnett, C.H.J. Davies, X. Ma, Scripta Mater. 52 (2005) 627–632.
[4] Z. Wu, W.A. Curtin, Nature 526 (2015) 62–67.
[5] Z. Wu, R. Ahmad, B. Yin, S. Sandlöbes, W.A. Curtin, Science 359 (2018) 447–452.
[6] W.B. Hutchinson, M.R. Barnett, Scripta Mater. 63 (2010) 737–740.
[7] J.-Y. Wang, N. Li, R. Alizadeh, M.A. Monclús, Y.W. Cui, J.M. Molina-Aldareguía, J. LLorca, Acta Mater. 170 (2019) 155–165.
[8] S. Ando, M. Tsushida, H. Kitahara, Materials Science Forum 706– 709 (2012) 1122–1127.
[9] H.-S. Jang, B.-J. Lee, Scripta Mater. 160 (2019) 39–43.
[10] J. van der Planken, A. Deruyttere, Acta Metall. 17 (1969) 451–454.
[11] S.R. Agnew, M.H. Yoo, C.N. Tomé, Acta Mater. 49 (2001) 4277–4289.
[12] S.R. Agnew, J.A. Horton, M.H. Yoo, Metall. Mater. Trans. 33 (2002) 851–858.
[13] M. Lentz, M. Klaus, I.J. Beyerlein, M. Zecevic, W. Reimers, M. Knezevic, Acta Mater. 86 (2015) 254–268.
[14] Y. Chino, M. Kado, M. Mabuchi, Acta Mater. 56 (2008) 387–394.
[15] Y. Chino, M. Kado, M. Mabuchi, Mater. Sci. Eng., A 494 (2008) 343–349.
[16] Y. Chino, K. Sassa, M. Mabuchi, Mater. Sci. Eng., A 513–514 (2009) 394–400.
[17] D. Zhang, H. Wen, M.A. Kumar, F. Chen, L. Zhang, I.J. Beyerlein, J.M. Schoenung, S. Mahajan, E.J. Lavernia, Acta Mater. 120 (2016) 75–85.
[18] D. Zhang, L. Jiang, X. Wang, I.J. Beyerlein, A.M. Minor, J.M. Schoenung, S. Mahajan, E.J. Lavernia, J. Mater. Res. 34 (2019) 1542–1554.
[19] G.H. Huang, D.D. Yin, J.W. Lu, H. Zhou, Y. Zeng, G.F. Quan, Q.D. Wang, Mater. Sci. Eng., A 720 (2018) 24–35.
[20] K. Hantzsche, J. Bohlen, J. Wendt, K.U. Kainer, S.B. Yi, D. Letzig, Scripta Mater. 63 (2010) 725–730.
[21] S. Sandlöbes, S. Zaefferer, I. Schestakow, S. Yi, R. Gonzalez-Martinez, Acta Mater. 59 (2011) 429–439.
[22] S. Sandlöbes, M. Friák, S. Zaefferer, A. Dick, S. Yi, D. Letzig, Z. Pei, L.-F. Zhu, J. Neugebauer, D. Raabe, Acta Mater. 60 (2012) 3011–3021.
[23] S. Sandlöbes, M. Friák, J. Neugebauer, D. Raabe, Mater. Sci. Eng., A 576 (2013) 61–68.
[24] H. Rikihisa, T. Mori, M. Tsushida, H. Kitahara, S. Ando, Mater. Trans. 58 (2017) 1656–1663.
[25] K. Takemoto, H. Rikihisa, M. Tsushida, H. Kitahara, S. Ando, Mater. Trans. 61 (2020) 935–940.
[26] L. Gao, R.S. Chen, E.H. Han, J. Alloys Compd. 472 (2009) 234–240.
[27] B.Q. Shi, R.S. Chen, W. Ke, Mater. Sci. Eng., A 560 (2013) 62–70.
[28] C. Zhao, Z. Li, J. Shi, X. Chen, T. Tu, Z. Luo, R. Cheng, A. Atrens, F. Pan, Journal of Magnesium and Alloys 7 (2019) 672–680.
[29] S. Sandlöbes, S. Zaefferer, I. Schestakow, S. Yi, R. Gonzalez-Martinez, Acta Mater. 59 (2011) 429–439.
[30] Standard Test Methods for Tension Testing of Metallic Materials.
[31] F. Bachmann, R. Hielscher, H. Schaeben, Solid State Phenom. 160 (2010) 63–68.
[32] C. Pradalier, P.-A. Juan, R.J. McCabe, L. Capolungo, Integrating Materials and Manufacturing Innovation 7 (2018) 12–27.
[33] C.N. Tomé, R.A. Lebensohn, (2004).
[34] R.A. Lebensohn, C.N. Tomé, Acta Metall. Mater. 41 (1993) 2611–2624.
[35] I.J. Beyerlein, C.N. Tomé, Int. J. Plast. 24 (2008) 867–895.

[36] M. Knezevic, I.J. Beyerlein, Adv. Eng. Mater. 20 (2018) 1700956.
[37] U. Essmann, H. Mughrabi, Philos. Mag. A 40 (1979) 731–756.
[38] F. Kocks, H. Mecking, Prog. Mater. Sci. 48 (2003) 171–273.
[39] Z.S. Basinski, Scripta Metall. 8 (1974) 1301–1307.
[40] G.C. Kaschner, C. Tomé, Mater. Sci. Forum (2005) 495–497, 1001–1006.
[41] G. Proust, C.N. Tomé, G.C. Kaschner, Acta Mater. 55 (2007) 2137–2148.
[42] Z.X. Wu, Y.W. Zhang, D.J. Srolovitz, Acta Mater. 57 (2009) 4508–4518.
[43] M. Bönisch, Y. Wu, H. Sehitoglu, Acta Mater. 153 (2018) 391–403.
[44] Z.-H. Jin, P. Gumbsch, K. Albe, E. Ma, K. Lu, H. Gleiter, H. Hahn, Acta Mater. 56 (2008) 1126–1135.
[45] F. Wang, S.R. Agnew, Int. J. Plast. 81 (2016) 63–86.
[46] F. Wang, K. Hazeli, K.D. Molodov, C.D. Barrett, T. Al-Samman, D.A. Molodov, A. Kontsos, K.T. Ramesh, H. el Kadiri, S.R. Agnew, Scripta Mater. 143 (2018) 81–85.
[47] M.D. Sangid, T. Ezaz, H. Sehitoglu, Mater. Sci. Eng., A 542 (2012) 21–30.
[48] L. Rémy, Acta Metall. 25 (1977) 711–714.
[49] Y.T. Zhu, X.L. Wu, X.Z. Liao, J. Narayan, L.J. Kecskés, S.N. Mathaudhu, Acta Mater. 59 (2011) 812–821.
[50] S. Ni, Y.B. Wang, X.Z. Liao, R.B. Figueiredo, H.Q. Li, S.P. Ringer, T.G. Langdon, Y. T. Zhu, Acta Mater. 60 (2012) 3181–3189.
[51] P. Chen, F. Wang, B. Li, Acta Mater. 164 (2019) 440–453.
[52] C.S. Roberts, Magnesium and its Alloys, Wiley, 1960.
[53] H. Yoshinaga, R. Horiuchi, Transactions of the Japan Institute of Metals 4 (1963) 1–8.
[54] N. Ansari, R. Sarvesha, S.Y. Lee, S.S. Singh, J. Jain, Mater. Sci. Eng., A 793 (2020) 139856.
[55] M. Ardeljan, I.J. Beyerlein, B.A. McWilliams, M. Knezevic, Int. J. Plast. 83 (2016) 90–109.
[56] M. Risse, M. Lentz, C. Fahrenson, W. Reimers, M. Knezevic, I.J. Beyerlein, Metall. Mater. Trans. 48 (2017) 446–458.
[57] S. Sandlöbes, M. Friák, S. Korte-Kerzel, Z. Pei, J. Neugebauer, D. Raabe, Sci. Rep. 7 (2017) 1–8.
[58] I.J. Beyerlein, R.J. McCabe, C.N. Tomé, J. Mech. Phys. Solid. 59 (2011) 988–1003.
[59] N. Stanford, R. Cottam, B. Davis, J. Robson, Acta Mater. 78 (2014) 1–13.
[60] A. Kula, X. Jia, R.K. Mishra, M. Niewczas, Int. J. Plast. 92 (2017) 96–121.
[61] S.R. Niezgoda, A.K. Kanjarla, I.J. Beyerlein, C.N. Tomé, Int. J. Plast. 56 (2014) 119–138.
[62] M. Knezevic, I.J. Beyerlein, D.W. Brown, T.A. Sisneros, C.N. Tomé, Int. J. Plast. 49 (2013) 185–198.